IOP Publishing Phys. Med. Biol. 63 (2018) 185004 (13pp) https://doi.org/10.1088/1361-6560/aadb3b

Physics in Medicine & Biology

IPEM Institute of Physics and Engineering in Medicine

RECEIVED
18 January 2018

REVISED
11 August 2018

ACCEPTED FOR PUBLICATION
17 August 2018

PUBLISHED
10 September 2018

PAPER

Design and performance of the micro-dose calibrator

Stephen Adler[1,3] and Peter Choyke[2]

[1] Clinical Research Directorate/Clinical Monitoring Research Program, Leidos Biomedical Research, Inc., NCI Campus at Frederick, Frederick, Maryland 21702, United States of America
[2] Molecular Imaging Program, National Cancer Institute, National Institutes of Health, Bethesda, MD, United States of America
[3] Author to whom any correspondence should be addressed.

E-mail: stephen.adler@nih.gov

Keywords: dose calibrator, coincidence detection, segmented well counter, micro-dose calibrator, well counter

Supplementary material for this article is available online

Abstract

A new class of dose calibrator called a micro-dose calibrator, designed to measure radioactivity rates in the range between 1 kBq up to 370 kBq, has been designed and an 8 NaI(Tl)/photo multiplier tube (PMT) module prototype built to evaluate its performance. The design of the micro-dose calibrator is based on the concept of a segmented well counter. By segmenting a single crystal well counter into multiple crystals or segments, with each segment operated and read out independently, one can extend the operational range of a standard single crystal well counter while maintaining its accuracy and spectrographic capabilities. The micro-dose calibrator is operated in *N*-fold coincidence mode to ensure that a single radioactive decay resulting in multiple segments detecting gamma ray events are counted as a single decay. The N fold coincidence detection is achieved using a pipeline coincidence processing algorithm implemented in software as part of a multi-threaded acquisition system. A tri-functional model pulse pileup dead time correction is applied to extend the operational range of the micro-dose calibrator. The micro-dose calibrator achieved an operation range between 1 kBq up to 3.4 MBq for ^{18}F with a 1% linearity precision using a 60 s integration time window. Over a 9 d period, a daily count rate measure of a ^{137}Cs point source had a coefficient of variation of 0.17% with only one high voltage calibration performed on day 0. The central 20 mm up to 35 mm axial length in the sample well showed less than 1% change in count rate depending on the radionuclide. Using a 0.5 ml insulin syringe, a volume of dose between 0.13 ml up to 0.50 ml showed less than 1% deviation from volumetric linearity. A 20 cc scintillation vial showed similar volumetric linearity performance for radionuclide solution volumes between 4 cc up to 20 cc.

Introduction

In the field of nuclear medicine and in the study of radioligands, a dose calibrator is used to measure the amount of radioactivity used to inject a patient or the activity used to study a radioligand in either a cell binding study, bio-distribution or other bio-efficacy studies. Standard dose calibrators are designed using an ionization chamber which allows one to measure with 10% accuracy doses up to 3.7 GBq (100 mCi) (Kowalsky *et al* 1977). The issue at hand is how well an ionization chamber class dose calibrator can measure with 1% accuracy doses which are commonly used in pre-clinical studies. These doses range from 37 kBq (1 μCi) up to 370 kBq (10 μCi) for organ tissue bio-distribution studies and up to 100 MBq (2.7 mCi) for imaging studies. Lower doses used to calibrate single crystal NaI well counters used in gamma counters can go as low as 3.7 kBq (100 nCi). These doses are not measured directly using a standard ionization chamber dose calibrator, but require one to use dilution methods instead, which can be subject to human error.

The other dose measurement device which can measure sub 37 kBq doses with great accuracy is a well counter (Anger 1951) which use a scintillation crystal, typically a thallium doped sodium iodide crystal, NaI(Tl), and is read out using a photomultiplier tube (PMT). With the ability of a well counter to count individual gamma emissions, the sensitivity of the instrument can reach as low as a few Becquerels, depending on the background count rate. Because of the very high sensitivity of the scintillation crystal, the ability of the crystal to measure high rates starts to saturate around 37 kBq (Zanzonico 2008).

Another problem with using a well counter as a dose measurement device is the sampling well is very small, typically 2 cm in diameter and 4 cm well depth. This restricts one to measuring volumes of activity which can only fit inside the small sampling well, typically a few cc's in small vials. The ability to measure the dose in a syringe, ready to be injected into an animal cannot be done. If one does use a 1.5 cc vial to measure a dose, then a volume correction is typically needed due to the geometrical dependence of well counter. These corrections can be as large as 20% and accurate knowledge of the volume will be required to apply a volumetric correction (Ten Haaf and Verheijke 1976).

Because of the difficulty in making low dose measurements, a new class of dose calibrator, called a micro-dose calibrator, has been designed specifically to address the ability to measure a dose of activity in the range of 1 kBq (27 nCi) up to 370 kBq (10 μCi) with less than 1% deviation from linear response. The performance testing of the micro-dose calibrator will focus on the NRC Dose Calibrator Quality Control Information Notice 93-10 (NRC 1993), which describes four tests, those being constancy, accuracy, linearity and geometry. The details of how these tests were performed will be discussed later. Factors which affect these tests, such as energy resolution of the NaI(Tl) and PMT stability tests are also covered. Of the four tests, the accuracy tests could not be performed for which reasons will be discussed later.

Materials and methods

Description

The micro-dose calibrator design is inspired by the concept of a segmented well counter, in which one takes a single scintillation crystal (typically NaI(Tl)) and segments it into multiple crystals, with each crystal being readout individually through its own electronic readout channel. The factor which limits the activity range of a scintillation crystal is the pulse pileup dead time driven by its scintillation light decay time. By segmenting the single crystal design into multiple crystals, the pulse pileup problem is reduced by the number of segments of the segmented well counter. The more segments, the higher the range of activity the segmented well counter can reach.

The segmented design introduces one problem which is counting decays in which multiple crystals record an event at the same time. Due to the multiplicity of gamma rays emitted in a single decay in many radionuclides, or due to Compton scatter events in which a single gamma ray can scatter from one crystal segment into another, one falls into the trap of over counting decays. To address this, a software-based pipeline coincidence detection capability has been designed into the data processing chain with the ability to tag events in which multiple detectors are hit at the same time caused by a single decay.

A prototype micro-dose calibrator has been built using eight custom made thallium doped sodium iodine (NaI(Tl)) crystals coupled to a photo multiplier tube (PMT) from Saint–Gobain Crystals (Hiram, Ohio). The NaI(Tl) crystal and PMT assembly is referred to as a NaI/PMT detector module. The individual NaI(Tl) crystals are designed in the shape of an isosceles trapezoid. With the 8 trapezoid shaped detector modules assembled, they form an octagon shaped well with a sampling well bore 50.8 mm (2.0″) in diameter from face to face and 10 cm (3.94″) deep. The detector module is 25.4 mm (1″) thick providing about a 60% absorption efficiency for 500 keV gammas (Saint–Gobain Crystals 2009). The NaI(Tl) crystal is directly light coupled to a 19.05 mm (0.75″) diameter Hamamatsu (Hamamatsu, Japan) R1166 PTM at the base of the crystal.

The PMTs are operated using electronic modules purchased from CAEN Electronics (Viareggio, Italy). These include PMT high voltage controllers, 250 M sample s^{-1} digitizers and fiber optic data bus interface to handle the required data bandwidth to operate all 8 detector modules at 300 kHz. The digitizers provide firmware with a constant fraction discriminator triggering feature and generates a data packet for each pulse signal containing the pulse area and time. Refer to figure 1 for photographs of the 8 NaI/PMT detector module assembly and associated readout electronics.

The micro-dose calibrator shown in the photos in figure 1 were taken without the presence of lead shielding in a lab where the initial assembly and software development was done. The data taken for all the tests reported below were done in the NCI Molecular Imaging Program animal lab where the micro-dose calibrator was installed behind proper shielding to reduce the ambient background radiation which could affect the performance of the instrument.

Software was developed to coordinate the operation of the electronic modules, provide calibration functionality, run the pipeline coincidence tagging algorithm, apply a dead time correction and display the activity rates of the dose placed inside the sampling well in real time. Refer to the supplemental material (stacks.iop.org/PMB/63/185004/mmedia) for a full description of the detector module, readout electronics and operating software inculding the pipeline coincidence tagging algorithm.

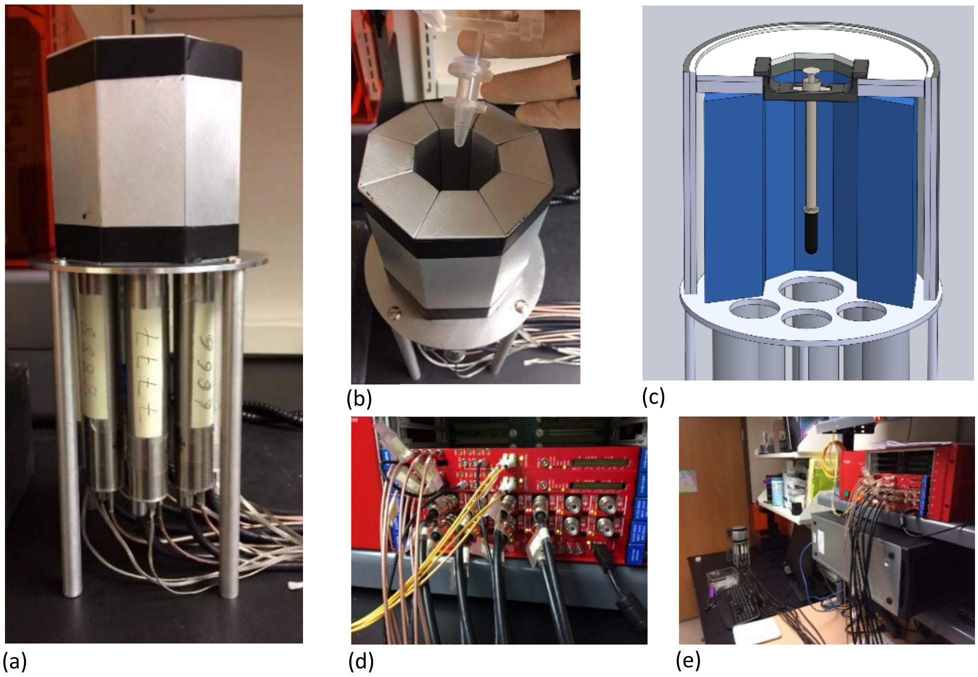

Figure 1. Figures (a) and (b) are photographs of the assembled NaI/PMT modules forming the octagon shaped segmented micro-dose well counter. Figure (c) is a cutout view of the 3D CAD model of the micro-dose calibrator with a syringe placed in the sampling well. The CAD model includes the lead shielding surrounding the crystal module in blue. Figure (d) is a photograph of the CAEN VME modules, V1725, V6533 and the V1718 operating in a VME crate. Figure (e) is a photograph of the VME create in the foreground, NaI/PMT detector modules in the background and associated HV and signal cabling connecting the two.

For the benefit of clarifying the data presented herein, when referring to the count rate measured by the micro-dose calibrator, the term correlated count rate is used. When applying the *N*-fold coincidence tagging algorithm, the count rate is broken down into the count rate in which uniquely single events are detected (1-fold coincidences), the count rate in which two detector coincidences are detected (2-fold coincidences), all the way up to the count rate for 8 detector coincidences or (8-fold) coincides. The correlated event rate is the sum of all *N*-fold coincidence rates. This is different than summing the individual events rates from each detector module independently, which is what is termed uncorrelated count rate. All references to count rates will be to correlated count rates, not uncorrelated.

PMT high voltage calibration

A high voltage calibration algorithm was developed to determine the high voltage settings for each PMT using a target mean voltage which would result in equal anode signal amplitudes across all 8 PMT channels. Using a radionuclide which has a well-defined photo peak, such as ^{137}Cs or ^{22}Na, a voltage scan is performed which measures the location of the photopeak in the resulting energy spectra for a given voltage setting. Because of the exponential nature of the gain response to the applied high voltage (Knoll 2010), the response curve is then fit with the following log function

$$V(P,\alpha,\beta,\gamma) = \ \alpha + \ \beta \log P + \gamma(\log P)^2 \tag{1}$$

where V is the high voltage setting, P is the photo peak channel and α, β and γ are the polynomial parameters determined using a non-linear fitting algorithm (James and Roos 1975). Using the fit response function unique to each PMT channel $(\alpha_i, \beta_i, \gamma_i)$, one then generates a list of photo peak channels P_i for the target high voltage V_T. Next one calculates the mean photo peak channel $\bar{P} = \ \sum {}^{P_i}\!/_{N}$ and from this mean, one calculates voltage settings

$$V_i = V\left(\overline{P},\alpha_i,\ \ \beta_i,\ \ \gamma_i\right) \tag{2}$$

which generates the list of individual high voltage settings for each detector module with a mean equal to the target high voltage V_T.

The high voltage calibration aligns the photo peaks of each detector modules to within 1% or 2% of each other. To obtain a higher precision photo peak alignment, a second order calibration is done by generating separate ADC bin to keV energy scale conversion factors for each detector module. This is done by fitting the photopeak in the spectra with a second-degree polynomial function and using the apex location of the polynomial to calculate the conversion factor

$$W_i = E/P_i \tag{3}$$

where W_i is the conversion factor for detector module i in units of keV/bin, E is the photopeak energy in keV of the source used to calibrate the detector modules, in this case 661 keV when using a ^{137}Cs calibration source, and P_i is the peak channel of the photopeak as measured by the 2nd degree polynomial fit. The conversion factor W_i can be interpreted as the bin width in keV of the energy spectra graph for detector module i.

Pulse pileup dead time correction

A pulse pileup dead time correction was developed to correct for the non-linear response at the higher rates of operation of the micro-dose calibrator. The live time fraction model, where live time fraction =1—dead time fraction, is broken down into three distinct transitional function models depending on the rate of operation of the micro-dose calibrator. These are

$$\begin{array}{lr} L = 1 & r < R_{c2q} \\ L = 1 - \alpha\left(r - R_{c2q}\right)^2 & R_{c2q} < r < R_{q2l} \\ L = \beta + \gamma\left(r - R_{q2l}\right) & r > R_{q2l} \end{array} \tag{4}$$

where L is the live time fraction and used as a correction factor applied to the correlated count rate. r is the raw correlated count rate, R_{c2q} is the transition rate between the constant and quadratic function model, R_{q2l} is the transition rate between the quadratic and linear function model, α is the quadratic parameter and β and γ are the linear parameters. At low rates, below R_{c2q}, the pulse pileup live time correction is deemed negligible and no correction is applied, thus the live time fraction correction fraction is equal to unity. When the correlated count rate crosses the R_{c2q} threshold, the live time fraction model takes on a quadratic form defined by α. Once the correlated event rate crosses the R_{q2l} rate threshold, the live time fraction model becomes linear defined by β and γ. A further constraint on the model is that the transitional function model and its derivative be continuous at the transition rate thresholds of R_{c2q} and R_{q2l}. This constraint is built into the constant and quadratic functions at the R_{c2q} transition. For the R_{q2l} transition, using the boundary conditions between the two functions, a further set of constraint equations can be derived which are

$$\begin{array}{c} \gamma = 2\alpha\left(R_{q2l} - R_{c2q}\right) \\ \beta = 1 - \alpha\left(R_{q2l} - R_{c2q}\right)^2. \end{array} \tag{5}$$

Therefore, the transitional model is determined by just three parameters, α, R_{c2q} and R_{q2l}.

The live time correction calibration is performed by filling a 1.5 ml polypropylene centrifuge vial with a 0.5 ml solution containing 3.7 MBq (100 μCi) of ^{18}F. The vial is then placed in the geometric center of the sampling well using a 3D printed vial holder designed for accurate and repeatable placement. Using the micro-dose calibrator GUI, a data collection is started which records all event rates, energy and coincidence time spectra every 60 s to a log file. The data collection proceeds for 48 h as the ^{18}F source decays through approximately 25 half-lives. From the log file, a decay curve is generated using the total correlated event count rate. The decay curve is fit with the following function

$$R\left(t\right) = Ae^{\frac{-t\ln(2)}{T_{1/2}}} + B \tag{6}$$

where A is the correlated count rate at $t = 0$, B is the background rate and $T_{1/2}$ is the half life of ^{18}F. The fit is performed using the data starting at the time at which the correlated count rate has fallen below 10 kcps (counts per second). Below this rate, pulse pileup effects affecting the live time of the micro-dose calibrator can be neglected. Using the half-life and background rate fit parameters resulting from the fit, one can then calculate the theoretical or expected rate throughout the 48 h of acquisition. The measured live time fraction is then generated by taking the ratio of the measured correlated activity rate over the expected correlated activity rate. This measured live time fraction is then fit to the tri-function transition live time model described earlier and the resulting three fit parameters, α, R_{c2q} and R_{q2l} are used when applying the dead time correction during the operation of the micro-dose calibrator.

Source activity calibration procedure

The method used to calibrate the micro-dose calibrator is done by using a Capintec dose calibrator (Florham Park, NJ) as the standard. A 37 MBq (1 mCi) sample of isotope is measured in the Captintec dose calibrator then diluted into 1 liter of solution. 1 cc volume is pipetted from the 1 L solution and placed in a 1.5 cc centrifuge vial and placed in the geometric center of the sampling well where a measurement is made of the correlated count rate. A calibration factor C

$$C = \frac{{}^{A_{capt}}\!/\!{}_{V_L}}{{}^{A_{\mu dc}}\!/\!{}_{V_{cv}}} \tag{7}$$

is calculated where A_{capt} and $A_{\mu dc}$ are the activities measured by the Capintec dose calibrator (in becquerels) and micro-dose calibrator (in cps) respectively and V_L and V_{cv} are the volumes of the 1 L dilution container and centrifuge vial respectively. Appropriate decay corrections are applied to the activity measurements and volumes are measured by weight. The calibration factor C has units of Bq/cps which, for the purpose of this constant, is used to convert the counts per second recorded by the micro-dose calibrator into the physical unit of disintegrations per second or Becquerel. The inverse of this constant is related to the efficiency of the micro-dose calibrator. The efficiency is defined as the count rate induced by gamma emissions measured by the micro-dose calibrator per unit disintegration

$$\begin{gathered} A_{\mu dc} = E\ B\ A_{Bq} \\ E = A_{\mu dc}/(B\ A_{Bq}) \\ E = 1/(B\ C) \end{gathered} \tag{8}$$

where E is the efficiency of the micro-dose calibrator, B, is the gamma emission branching fraction, A_{Bq} is the activity in Becquerels, $A_{\mu dc}$ the activity measured by the micro-dose calibrator in counts per second and C is the calibration constant from equation (7). Therefore, by measuring the calibration constant for a given radionuclide, one is in effect measuring the efficiency of the dose calibrator for that radionuclide as well when accounting for the gamma branching fraction.

Performance measurements

Energy and coincidence time resolution

Energy and coincidence time resolution measurements were made to measure the performance of the detector module. Energy resolution ($\Delta E\%$) is defined as the percentage ratio of the full width at half maximum (FWHM) of the photopeak to its mean energy value of the peak ($\overline{E_p}$).

$$\Delta E\% = \frac{\text{FWHM}}{\overline{E_p}} 100\%\,. \tag{9}$$

The timing resolution is defined as the FWHM of a distribution of time differences measured by two NaI/PMT detector modules.

The FWHM is measured using a polynomial fit to the peak of the gaussian distribution to measure the apex and its X axis location. Linear interpolation is used between histogram bins above and below the half maximum threshold to measure the width. See figures 2(a) and (b).

Constancy

To measure the stability of the detector modules and the constancy of the micro-dose calibrator between calibrations, a set of count rate, photopeak and energy resolution measurements were made daily over a period of 9 d with only one calibration performed on day 0. The measurements consisted of measuring the background count rate with no source inside the micro-dose calibrator, then placing a ^{137}Cs point source in the center of the micro-dose calibrator and measuring the count rate, the peak energy of the photopeak and the energy resolution. All measurements were made by collecting data for 1 min.

Source geometry dependence

Two studies were performed to measure the effects of varying the geometry of the source and its effects on the resulting count rate measured by the micro-dose calibrator. The first was to map out the axial sensitivity within the sampling well and the second was to study source geometry and its dependence on the count rate.

To measure the axial sensitivity of the micro-dose calibrator, 11 different radionuclides were placed at 5 mm steps along the vertical central axis of the micro-dose calibrator sampling well starting at the upper opening down to the bottom of the well. The 11 sources were ^{18}F, ^{22}Na, ^{54}Mn, ^{57}Co, ^{60}Co, ^{88}Y, ^{89}Zr, ^{133}Ba, ^{137}Cs, ^{203}Hg and ^{241}Am. The placement of the source was done with the help of a 3D printed scaffold and source holder which allowed for accurate and reproducible placement. The ^{18}F, and ^{89}Zr radionuclides were in liquid form. 1.5 cc vial was used to hold a 0.5 cc liquid sample of these two radionuclides. The other nine radionuclides were point sources encapsulated in a rectangular plastic container. The total correlated count rates as well as N fold coincidence count rates were recorded for each 5 mm step. The count rate was integrated for 1 min at each sampling step.

To process the data, a relative sensitivity factor was calculated by averaging the five vertical positions with the highest count rates and normalizing all the count rates to this average. To measure the vertical length in which the normalized sensitivity stays above 99%, one interpolates the top and bottom adjacent points which fall below 99% and take the distance between the two intersection points.

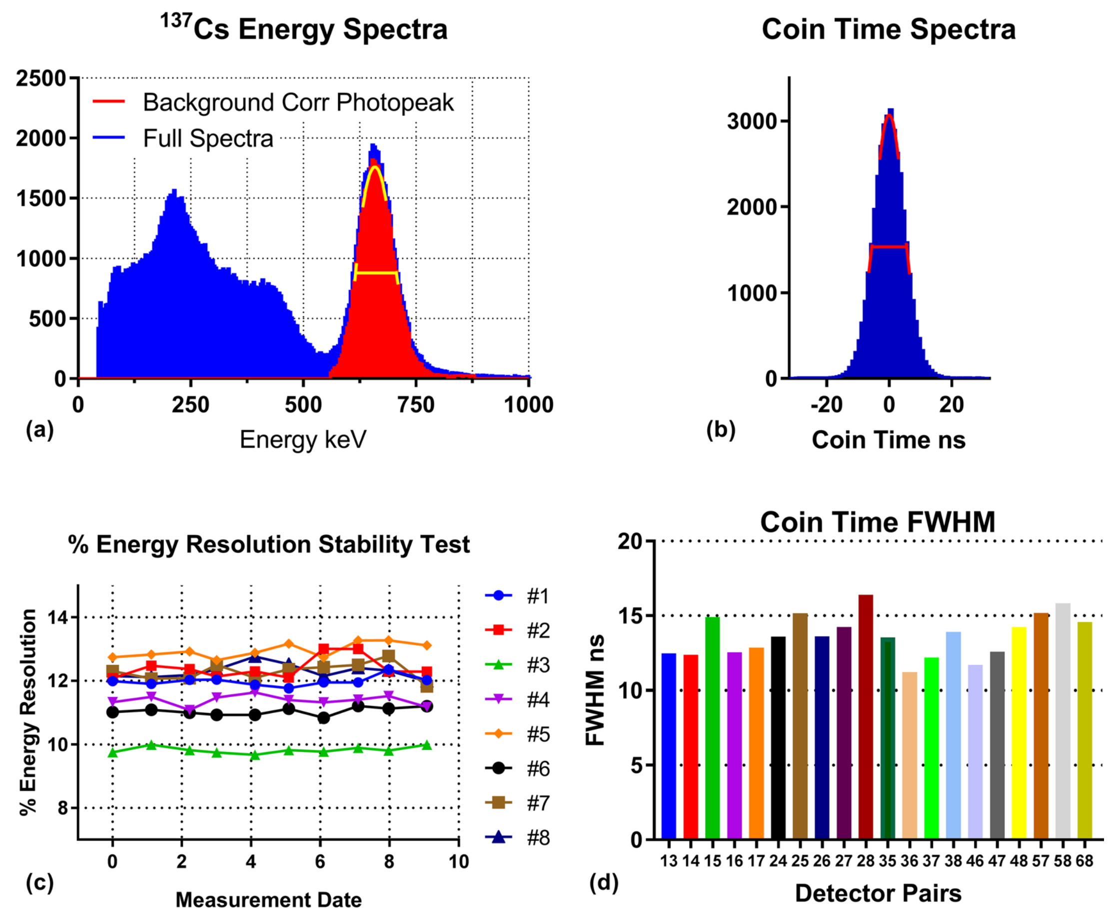

Figure 2. Energy and coincidence time resolution data. Figure (a) shows the energy spectrum of detector module #5, with the full spectrum drawn in blue while the background subtracted photopeak is drawn red. Overlaying the photopeak distribution are the peak fit using a 2nd order polynomial function and the FWHM interpolation lines used to calculate the % energy resolution. Figure (b) shows the coincidence time spectrum between detector modules #3 and #6 measured with a lower energy threshold set to 400 keV. Figure (c) shows a graph plotting the energy resolution data collected over 9 d and figure (d) shows a bar graph of the timing resolution measurements between all non-adjacent detector module pairs measured with the lower energy threshold set to 400 keV.

The fractional N-fold coincidence rate C_i per radionuclide is calculated using the formula

$$C_i = \frac{R_i}{\sum_i R_i} \tag{10}$$

where R_i is the N fold coincidence rate with R_1 being the unmatched singles rate, R_2 the two-fold coincidence rate, etcetera and $\sum_i R_i$ is the total correlated count rate.

To measure the geometrical dependence of the source on the count rate, a 0.5 ml insulin syringe and a 20 cc scintillation glass vial were fill with different volumes of solution containing either ^{18}F or $^{99\text{m}}$Tc and activity measurements were made for each volume of solution. The volume increments were 0.05 ml and 2 ml for the insulin syringe and 20 cc scintillation vial respectively.

Linearity

To measure the linearity of the micro-dose calibrator, 1 cc of solution containing 3.7 MBq (100 μCi) of ^{18}F was placed in the center of the sampling well and activity measurements were made every minute for 48 h. The tail of the resulting decay curve, as defined by the time at which the rate fell below 10 kcps, was fit with an exponential plus background function $R(t)$

$$R_{expected}\left(t\right) = Ae^{\frac{-\ln(2)t}{T_{1/2}}} + B \tag{11}$$

where the fitting parameters are A, the activity rate at $t = 0$, the half-life of the radionuclide $T_{1/2}$, and the background rate B. With the fit parameters determined, a theoretical function which covers the full range of the data collected can be formed. One can then measure the percent deviation from linearity using the expression

$$\Delta L\left(t\right)\% = \frac{R_{measured}(t)}{R_{\exp\,ected}(t)}100\% \tag{12}$$

Table 1. Micro-dose calibrator efficiency table.

Radionuclide	Gamma ray efficiency
^{18}F	0.665
^{68}Ga	0.543
^{89}Zr	0.263
^{99m}Tc	0.671
^{177}Lu	0.434

where $R_{measured}(t)$ is the dead time corrected correlated count rate using the dead time correction parameters measured using the calibration data set.

Results

Detector module performance and micro-dose calibrator efficiencies

The energy resolution was measured once a day over a period of 9 d to see if there were any near-term degradations in the energy resolution performance of the detector modules. Refer to figure 2(a) to see the typical energy spectra measured from a ^{137}Cs source and the resulting fit data used to measure the energy resolution. Over this period the average energy resolution was measured for each detector module. The detector module with the lowest energy resolution measurements was 9.8% ±0.1% and the highest was 13.0% ± 0.2%. The average energy resolution across all eight detector modules was 11.8% ± 1.0%. Refer to figure 2(c) to see a graph of the daily measurements made of the energy resolution for each detector module. The day to day variation for the individual detector modules had a coefficient of variation which ranged between a minimum of 1.1% and a maximum of 2.7%.

The coincidence time resolution data was taken by placing eight 10 cc syringes filled with an ^{18}F solution inside the sampling well taped to the surface of each detector module to provide greater detector pair module coverage than just placing one syringe in the center of the well. Preferably, a cylindrical ^{68}Ge phantom, which has an outer diameter similar in size to the inner diameter of the sampling well, would have been used, but none was available. The eight-syringe setup provided the needed data to measure the coincidence timing resolution. The lower energy threshold was set to 400 keV while the coincidence timing data was collected. Adjacent detector modules were excluded from the measurement data since the lower energy threshold of 400 keV eliminated scatter events which is the main mechanism which form coincidence events between adjacent detector modules. The coincidence time resolution between non-adjacent detector pairs varied from a minimum of 11.2 ns up to a maximum of 16.4 ns, with an average of 13.7 ns ±1.4 ns. Figure 2(b) is a plot of a typical coincidence time distribution spectrum and 2(d) is a bar graph of all non-adjacent detector pair timing resolution measurements.

Calibrations were performed on the micro-dose calibrator for five different radionuclides. From the calibrations, the efficiencies were determined using equation (8) and are listed in table 1. The efficiency varies from 0.671 for ^{99m}Tc down to 0.263 for ^{89}Zr.

Further detector module performance studies can be found in the supplemental material, which includes a non-standard method of decoupling the coincidence timing resolution into single detector module timing jitter measurements, scintillation light yield studies and correlations of timing resolution on light yield, high voltage settings and lower energy threshold settings.

Constancy

Figure 3 contain plots of the data collected over the 9 d constancy test period. Figure 3(a) shows a graph plotting the photopeak mean value for each detector module measured once a day over the 9 d period. The micro-dose calibrator underwent an energy calibration prior to the first photopeak measurement on day 0. The data show the stability of the detector modules and the magnitude of the high voltage drift. Figure 3(b) plots the coefficient of variation of the photopeak mean drift of the eight detector modules and figure 3(c) plots the percent mean deviation from the calibration setting of 661 keV. On average, the coefficient of variation drift is 0.065% per day, while the mean drift from the calibration setting of 661 keV remained under 0.5%. Figure 3(d) plots the daily measurements in counts per second, both signal plus background in red and just the signal in blue. From the signal data plotted in figure 3(d), the average activity over a 9 d period has a coefficient of variation of 0.17%.

Linearity

The linearity data are shown in figure 4. Data for both the pulse pileup dead time correction and the linearity results are presented. Figures 4(a) and (b) plot the raw correlated count rate decay curve along with the extrapolated or expected decay curve generated from the fit to the lower end of the raw decay curve starting at the time the count rate fell below 10 kcps. Figure 4(a) has a linear Y axis scale while figure 4(b) is logarithmic. On

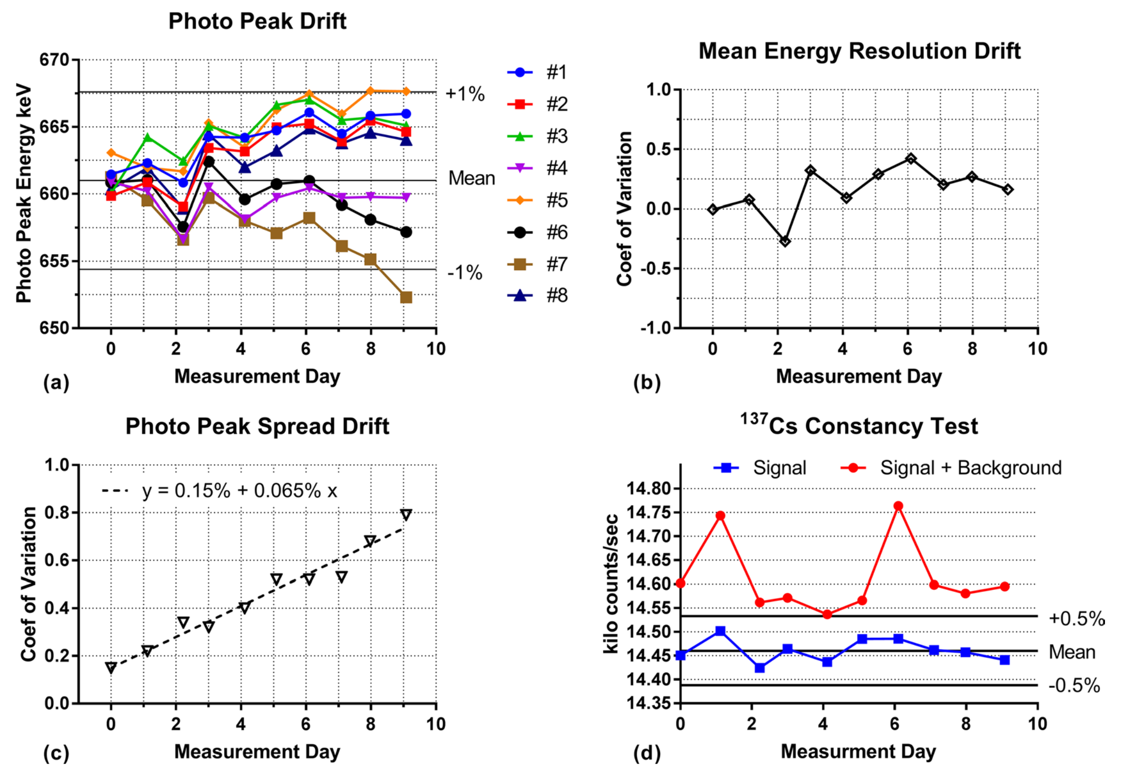

Figure 3. Constancy data plots. Figure (a) plots the photopeak energy as a function of measurement day for each detector module. Figure (b) plots the mean photopeak energy over the expected photopeak energy of 661 keV as a function of the measurement day. Figure (c) plots the coefficient of variation of the photopeaks which measures the daily drift of 0.065%. Figure (d) shows the main constancy measurement data. It is a plot of the variation in count rate for the ^{137}Cs source over the 9 d period showing a drift less than 0.5% with a coefficient of variation of 0.17%.

the linear scale graph, one can see the effects of the pulse pileup dead time while on the logarithmic scale graph, one can see the see the background contribution to the decay curve.

Figure 4(c) shows the results of the pulse pileup live time model plotting the fractional live time against the raw correlated event rate in cps. The tri-functional pulse pile up live time model described by equations (4) and (5) is superimposed to show the agreement of the model to the measured data over a raw correlated count rate up to 1.5 Mcps. Figure 4(d) shows the same data focusing on the low data rates up to 200 kHz. Figure 4(d) shows how well the quadratic and linear portions of the model fit the data. The plot also shows pulse pileup live time correction is about 2% at 200 kcps, while figure 4(c) shows the live time correction to be about 20% at 1.5 Mcps.

Two linearity data sets were collected and shown in figures 4(e) and (f). The first data set, dated July 16, was used to generate the model fit parameters and the second one dated July 28, was used to show proof of principle of the model. The fit parameters generated from the July 16 data set are $\alpha = -1.35 \times 10^{-12}$, $R_{c2q} = 12.3$ kcps and $R_{q2l} = 87.5$ kcps. The July 28 data set used the July 16 fit parameters to perform the pulse pile up dead time correction. The live time corrected correlated count rate fractional linearity deviation, (corrected rate/expected rate), is plotted in figure 4(e) showing a deviation of less than ±1% up to 3.4 MBq. The July 28 data set used to measure reproducibility is superimposed. Figure 4(f) graphs are of the same data, except the X axis covers the low rate range of 1 Bq up to 370 kBq (10 μCi) and plotted in log form. With the live time model applied to the correlated count rate shown in figure 4(f), deviation from linearity drops down to sub 0.2% at activity rates greater than 37 kBq (1 μCi) up to 370 kBq (10 μCi) and beyond. From the same figure, one can infer the lower ±1% limit of accuracy approaches 1 kBq.

Geometry

Figures 5 and 6 and table 2 detail the results of the geometry tests described in the methods section. The first set of measurements, shown in figure 5, were designed to measure the axial sensitivity variation within the microdose calibrator sampling well. The goal was to measure the axial length in the center of the sampling well in which the sensitivity would deviate less than ±1%. The resulting data show that there are two classes of radionuclides which have different sensitivity responses. Those which have a high branching fraction in which a positron is emitted and those with no positron emitted or if they do, have a low branching fraction. The sources which do not emit a measurable emission rate of positrons tend to have ±1% sensitivity lengths of about 20 mm, while those which do, have ±1% sensitivity lengths of up to 35 mm. Table 2 lists the ±1% sensitivity lengths for the

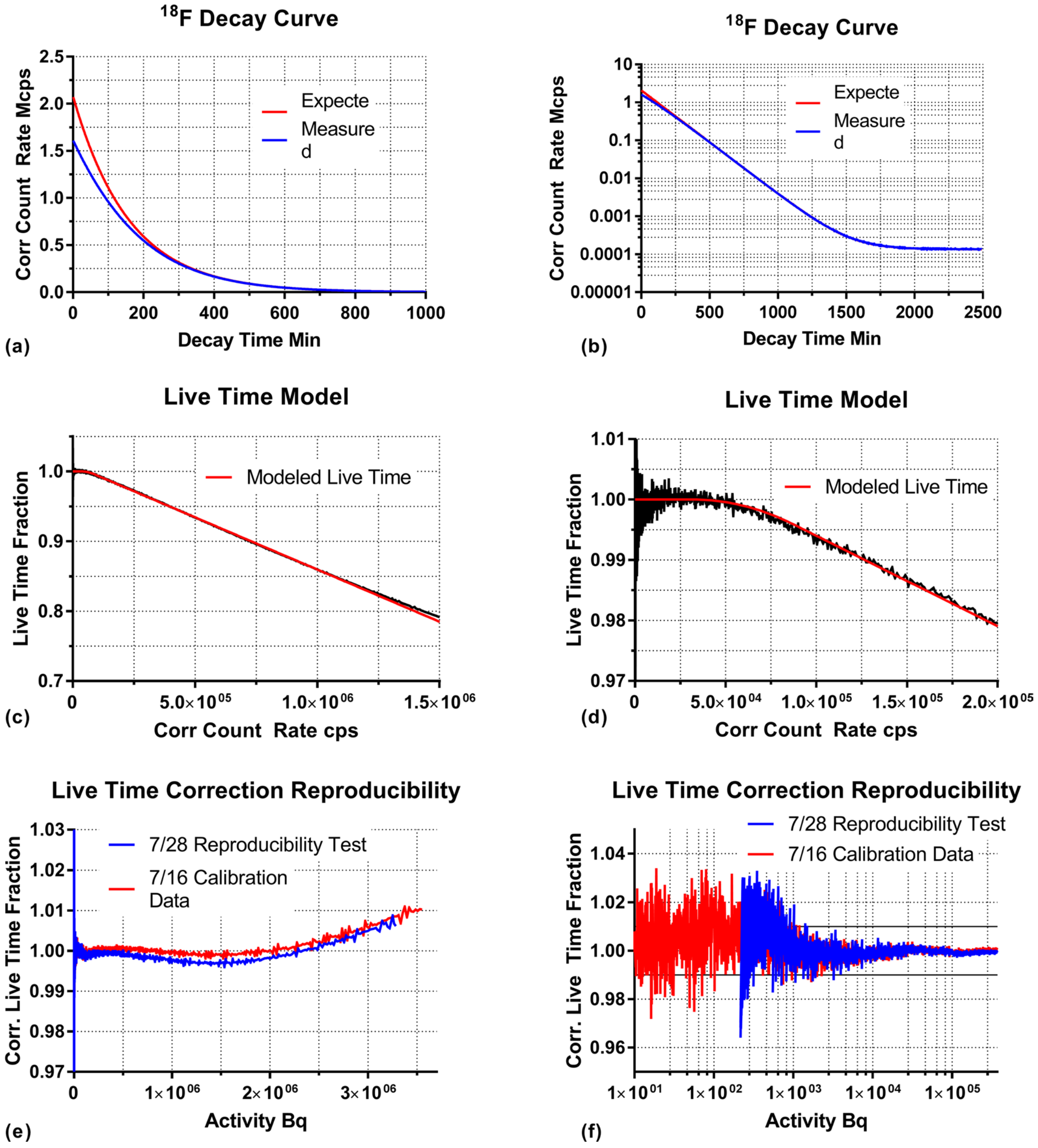

Figure 4. Linearity data and results from the fit to the pulse pileup equation described by equations (4) and (5). Figures (a) and (b) plot the expected and measured correlated count rate decay curves with figure (a) plotting the data on a *Y* axis linear scale and figure (b) on a logarithmic scale. Figures (c) and (d) plot the measured over expected rate and superimposed on the figures is the result of pulse pileup fit (equations (4) and (5)) with the resulting fit parameters of $\alpha = -1.35 \times 10^{-12}$, $R_{c2q} = 12.32$ Kcps and $R_{q2l} = 87$ Kcps. Figure (d) shows the same data below 200 kcps to show how well the model fits the pulse pile up response of the mico-dose calibrator. Figures (e) and (f) plot the dead time corrected over expected rate. The July 16 data set was used to generate the fit parameters and the July 28 confirmation data shows the proof of principle of the model. The pulse pileup dead time model provides a correction which keeps the linearity within ±1% up to 3.4 MBq.

isotopes used to measure this length. Figures 5(a) and (c) plot the relative sensitivity as a function of the vertical placement of the radionuclides inside the micro-dose calibrator's sampling well. A red line is drawn between the two interception points where the sensitivity drops below 99%. The length of the line measures the ±1% sensitivity length. Figures 5(a) and (b) show data from positron emitting radioisotopes ^{18}F while figures 5(c) and (d) show data from the ^{137}Cs isotope which has a primary single gamma emission of 661 keV. Figures 5(b) and (d) plot the *N*-fold fractional coincidence rate up to 4-fold and 3-fold coincidences respectively. From the data shown, one can see the difference in axial response caused by the presence or absence of the predominant 2-fold coincidence rate caused by positrons emitted from the decay and their subsequent annihilation. In the absence of the positron, the *N*-fold fractional coincidence rate is independent of the axial position within the micro-dose calibrator sampling well (figure 5(d)). When a positron is emitted in the decay, one can see a strong dependence of the *N*-fold fractional coincidence rate on the axial position of the source with the $N >=2$-fold fractional coincidence rate maximizing at the center of the well, while the fractional singles rate (1-fold coincidence) is at a minimum when the source is at the center (figure 5(b)).

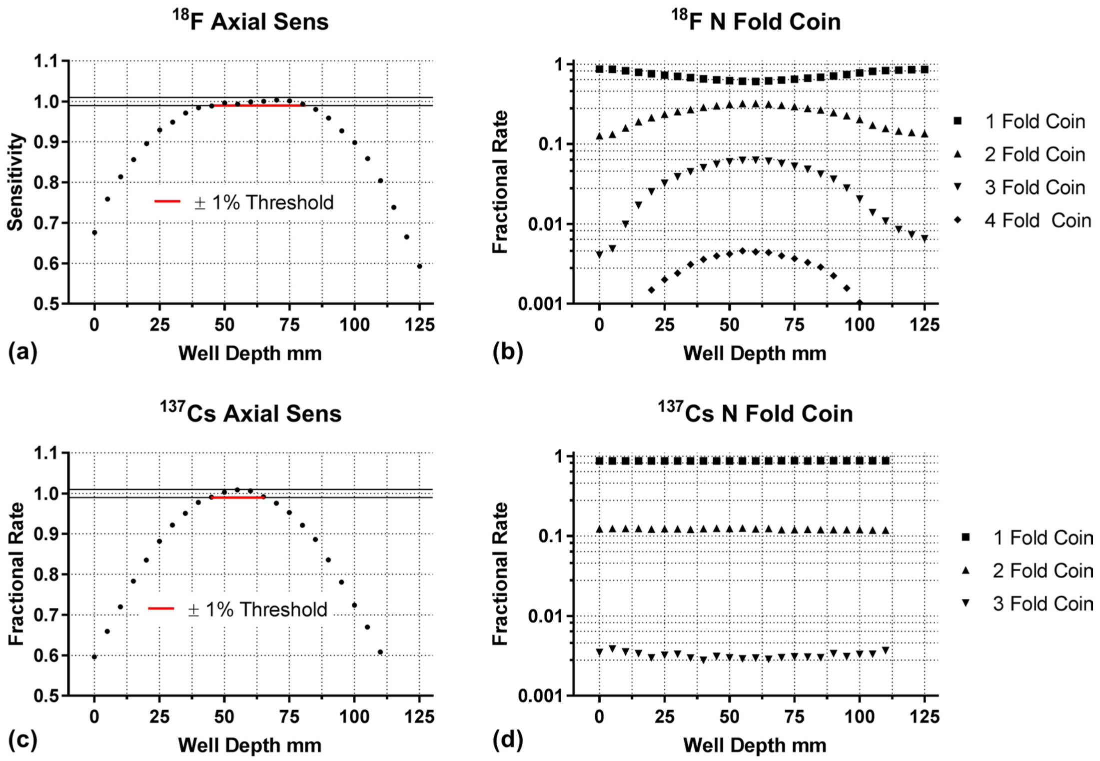

Figure 5. Axial sensitivity response measurements for ^{18}F and ^{137}Cs. The left column figures (a) and (c) show the relative sensitivity profile along the axial depth of the sampling well. The axial length in which the relative sensitivity is within ±1% is drawn in red. The right column figures (b) and (d) show the relative fractional coincidence rate dependence on the vertical axial profile inside the sampling well. To note, the ^{18}F radionuclide shows a high dependence of the fractional N fold coincidence rate on the position of the sample in the well. This is not the case for the non-positron emitting nuclide ^{137}Cs.

The results of the volumetric geometrical characterization of the micro-dose calibrator can be found in figure 6. Volumetric rate measurements were performed using a 0.5 ml insulin syringe and a 20 cc glass scintillation vial. Linearity plots and % deviation from linearity as a function of source volume are graphed and shown in the left and right columns of figure 6 respectively. With the 0.5 ml insulin syringe and 20 cc glass vial data shown in the top and bottom row of graphs respectively. Since the initial sets of measurements determining the ±1% sensitivity length showed a dependence on the radionuclide depending on whether it was a positron emitter or not, two radionuclides were used in the volumetric measurements, ^{18}F and ^{99m}Tc. The set of data which plots the activity rate as a function of volume, shown in figures 6(a) and (c), are fit with a linear function with a 0 intercept. The R^2 of the fit is greater than or equal to 0.999 79. The deviation from linear response as a function of volume is plotted in the graphs shown in figures 6(b) and (d). The data show that for the 0.5 ml insulin syringe, all volume measurements have less than a ±1% deviation from linearity for ^{18}F, and volumes greater than 2 cc in the 20 cc glass flask also had less than a ±1% deviation. For the ^{99m}Tc, insulin syringe volumes greater than 0.13 ml had linear deviations less than ±1% while 20 cc glass vial volumes greater than 4 cc had a linear divination less than ±1%.

Discussion

The prototype micro-dose calibrator, designed using the concept of a segmented well counter, has exceeded its goal of measuring small doses of radioactivity up to 370 kBq (10 μCi) within ±1% deviation from linear response by reaching up to 3.4 MBq (92 μCi). This was achieved with the use of the tri-functional pulse pileup dead time correction model described in the methods section. At 370 kBq (10 μCi), the dead time correction is only 2.5%, while at 3.4 MBq, the correction is 20%, which well within a range that a dead time correction can be suitably applied. The maximum data rate which the electronics can handle is about 3×10^6 data packets per second which is reached when about 4.5 MBq (122 μCi) of ^{18}F is placed in the sampling well. This data bottleneck does not allow one to perform meaningful linearity tests much above 3.7 MBq (100 μCi).

The other dose calibrator standard performance measurements, that of constancy and geometry, also demonstrated sub ±1% accuracy, with the constancy measuring a coefficient of variation of 0.17% over a 9 d period with only one calibration performed on the micro-dose calibrator on day 0. Related to constancy are the PMT voltage stability tests which was determined by tracking the 661 keV photopeak of a ^{137}Cs point source over the 9 d

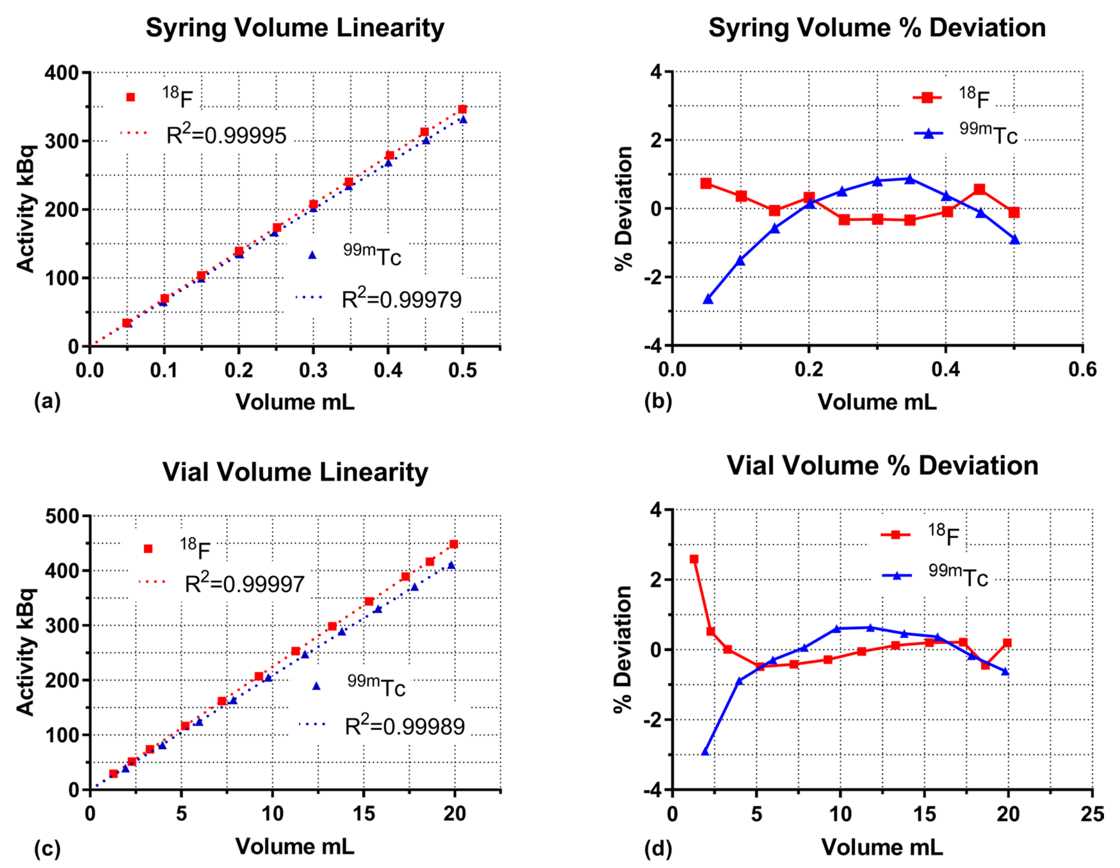

Figure 6. The graphs present the results from the volumetric linearity tests, measuring the accuracy of the micro-dose calibrator against changes of the source volume and geometry. Data taken using a 0.5 cc insulin syringe and a 20 cc scintillation glass vial are shown in top and bottom rows respectively. Because the micro-dose calibrator has a different axial response depending on whether there is a positron emitted in the decay scheme of the nuclide, both ^{18}F and ^{99m}Tc sources were used in these measurements. The results demonstrate the ability of the micro-dose calibrator to measure a dose to within a 1% accuracy for the full 0.5 cc volume range of the insulin syringe for ^{18}F and a 0.35 cc volume range for ^{99m}Tc. The volume ranges are 17.5 cc and 16 cc for the 20 cc glass bottle for ^{18}F and ^{99m}Tc respectively.

period. Despite the high voltage drift, leading to a drift in the photopeak energy of up to ±1% for some modules, which in turn changes the effective lower energy threshold for each detector module, the total background subtracted count rate from the ^{137}Cs source had a coefficient of variation of 0.17% over the 9 d period demonstrating the robustness of the micro-dose calibrator.

With respect to the results of the geometry tests, one of the key measurement parameters was to determine the axial length within the sampling well of the micro-dose calibrator which would be count rate insensitive to positional variations. The results show that for all the radionuclides tested, one has a length of 20 mm in which the count rate will vary less than 1%. For positron emitting radioisotopes, of which ^{18}F is the most widely used, this length extends to about 35 mm. This is due to the >=2 fold coincidence axial response of the micro-dose calibrator from the presence of back to back gammas resulting from positron/electron annihilation. The 20 mm up to 35 mm length of sub ±1% activity rate variation then lends the micro-dose calibrator to be able to measure within this ±1% accuracy range, different volumes of activity in containers commonly used in pre-clinical studies, like the 0.5 ml insulin syringe or 20 cc scintillation glass vial. The choice of using a 0.5 ml syringe and a 20 cc scintillation vial to study the volumetric linearity response of the micro-dose calibrator was done because the two devices span a good range in object width and length dimensions, with the 0.5 ml insulin syringe having an inner diameter of 3.6 mm and length of 50 mm and the 20 cc scintillation vial an inner diameter of 25 mm and length of 45 mm. With the syringe and 20 cc vial used to measure the volumetric linearity, the two disparate diameters indicate that any other objects with a diameter between 3.6 mm and 25 mm and a length up to 45 mm should have a ±1% variation from volumetric linearity. To note, the volume range for the 0.5 ml insulin syringe translates to a vertical length range of up to 50 mm and the 20 cc glass vial having a vertical length range of up to 45 mm. Therefor the volume lengths of the syringe and glass vial of 50 mm and 45 mm respectively are far greater than the 20 to 35 mm stability lengths measured with 0.5 cc solution in a 1.5 cc micro-centrifuge vials or point sources, yet even with the volume of activity lying outside the ±1% sensitivity boundaries, one is still able to make ±1% volumetric measurements. This is because one is integrating the sensitivity across the axial length which allows one to go

Table 2. List of radionuclides measured in the micro-dose calibrator. The first three in the list and in bold letters are positron emitters. The ±1% sensitivity length is listed along with the list of primary gamma ray energy and their percent emission rate.

Source	±1% sensitivity length mm	Primary Gamma Energy KeV (% emission rate)
^{18}F	35.4	511 (193.5%)
^{22}Na	34.9	511 (180.8%), 1274 (99.9%)
^{89}Zr	25.8	511 (45.5%), 909 (99.0%)
^{54}Mn	23.5	834 (99.9%)
^{57}Co	22.9	122 (85.6%), 136 (10.7%)
^{60}Co	23.4	1173 (99.9%), 1332 (99.9%)
^{88}Y	25.3	898 (93.7%), 1836 (99.2%)
^{133}Ba	25.8	81 (32.9%), 303 (18.3%), 356 (62.1%)
^{137}Cs	20.7	661 (85.1%)
^{203}Hg	21.4	279 (81.6%)
^{241}Am	19.8	60 (35.9%)

beyond the ±1% sensitivity length as measured by a point source. In this case, one can go up to 50 mm with the syringe and 45 mm with the 20 cc glass vial and stay within the ±1% sensitivity variation window.

To enable these accurate volumetric measurements, individually designed holders for the insulin syringe and 20 cc glass vial were made using a Formlabs (Boston MA) Form 2 SLA 3D printer. This achieved reproducible placement at the ±1% sensitivity depth within the micro-dose calibrator's sampling well.

The final major dose calibrator performance test, the accuracy test, could not be performed due to the lack of a precision calibration standard. An effort was made to contract NIST to make a standard for the micro-dose calibrator, but funding efforts failed. The method of calibration is done against a standard Capintec CRC-25R dose calibrator as describe in the methods section. Any variations in the dose measurements of the Capintec dose calibrator will have repercussions in the accuracy measurement of the micro-dose calibrator, therefore one cannot pin point the variability in accuracy to either the Capintec dose calibrator or the micro-dose calibrator. Funding efforts to contract NIST to make a proper calibration standard for the micro-dose calibrator continue and when successful, the accuracy test will be conducted.

To address the considerations which went into the design of the micro-dose calibrator, one should understand that the goal was not to design a 4π spherical detector which maximizes gamma ray detection efficiency. Instead it was designed to have good efficiency and be a useful instrument to measure radionuclide solutions of different volumes in an assortment of containers, these being 1.5 cc centrifuge vials, syringes, scintillation glass vials, etcetera. The intent was to take the standard well counter designed by Dr Anger (Anger 1951) back in the early 1950s and extend its count rate capability while at the same time be able to make these measurements on instruments and containers commonly used in the lab setting. Therefore, the thickness of the detector module was chosen to be 25.4 mm (1″). A typical crystal thickness (outer diameter–inner diameter) of a well counter is about 16 mm (.63″). The sampling well needed to be large enough to accommodate the containers, so a 50.4 mm (2″) inner diameter size was chosen for the sampling well and 100 mm (3.94″) its length. The ability to make accurate linear volumetric measurements without resorting to volume corrections is due to the through hole design of the sampling well. Ten Haaf *et al* (Ten Haaf and Verheijke 1976) were the first to study the performance of a well counter with a through hole design and its advantages in reducing the source volumetric dependence on the gamma ray detection efficiency.

The results of the energy and coincidence time resolution tests of the NaI/PMT detector module were not as good as expected. The mean energy resolution of 11.8% is greater than the average 7% energy resolution Saint–Gobain reported during their factory QA testing. Furthermore, the average timing resolution of 13.7 ns with a lower energy threshold setting of 400 keV as measured by two detector modules is greater than the 6 ns timing resolution reported by others (Derenzo *et al* 1979). With the average coincidence time resolution of 13.7 ns, the coincidence window is set to 60 ns such that one can tag over 99.7% (three sigma) of coincidence events. When discussing the poor energy resolution performance with the engineering team at Saint–Gobain, a spare detector module was sent back for analysis. Saint–Gobain adjusted their design by improving the insulation technique to ensure the performance does not degrade due to moisture absorbing into the crystal. Initial tests on the improved detector module has an energy resolution of 6.8%. The other detector modules will be sent back to Saint–Gobain for adjustment. This should improve the timing resolution and further studies will be performed to see how the linearity is affected at the 1.85 MBq (50 μCi) to 3.7 MBq (100 μCi) range of activities once all detector models have undergone this insulation fix.

Because the micro-dose calibrator relies on coincidence processing, a study of the randoms contribution to the coincidence rate was performed. The results showed a negligible contribution which is absorbed into the pulse pileup linearity correction model. Full details of the study are found in the supplemental material.

Conclusion

A first in class micro-dose calibrator, designed to bridge the measurement gap between a traditional single crystal well counter and an ionization chamber dose calibrator has been designed, and performance measurements have been made on a prototype built at the NCI Molecular Imaging Program laboratories. The micro-dose calibrator, using the concept of a segmented well counter in conjunction with N-fold coincidence event tagging, allows the device to have an operational range greater than that of the traditional single crystal NaI well counter. In this design, an 8-segment well counter, the activity range was extended up to 3.4 MBq with the help of a pulse pileup dead time correction model and keeping the linear response of the micro-dose calibrator within $\pm1\%$. The $\pm1\%$ sensitivity length measured by a point source along the center axis of the sampling well is between 20 mm and 35 mm depending on the radionuclide. Whereas the $\pm1\%$ volumetric sensitivity within the sampling well has a dimension of 45 mm along the central axis with a diameter of 25 mm. The micro-dose calibrator showed a coefficient of variation of 0.17% when measuring the rate of a ^{137}Cs source over a period of 9 d. Despite the non-optimal performance of the NaI/PMT detector design and the use of off the shelf electronics, the prototype 8 segment micro-dose calibrator demonstrated that using the design concept of a segmented well counter, one can build a micro-dose calibrator which has a much greater reach in dynamic range than the traditional single crystal well counter. This instrument allows one to make accurate dose measurements in the 1 kBq up to 3.4 MBq range which is ideal for bio-distribution studies.

The design of the micro-dose calibrator has been filed with the US Patent Office. The Technology Transfer Center of the National Cancer Institute is soliciting industry partners to commercialize the device.

Acknowledgments

The authors acknowledge Dr David Zimmerman, Project Leader, nuclear Medicine Standards of the NIST Radioactivity Group and his team for insightful discussions in low dose measurement techniques.

Funding

Funding for this research was provided by the National Cancer Institute Invention Development Fund.

We acknowledge partial support from Leidos Biomedical Research Inc. through the award of the 2017 Laboratory-Directed Exploratory Research Grant.

This project has been funded in whole or in part with federal funds from the National Cancer Institute, National Institutes of Health, under Contract No. HHSN261200800001E. The content of this publication does not necessarily reflect the views or policies of the Department of Health and Human Services, nor does mention of trade names, commercial products, or organizations imply endorsement by the US Government.

References

Anger H 1951 Scintillation counters for radioactive sample measurement *Rev. Sci. Instrum.* **22** 912–4
Derenzo S E, Budinger T F, Cahoon J L, Greenberg W L, Huesman R H and Vuletich T 1979 The donner 280-crystal high resolution positron tomograph *IEEE Trans. Nucl. Sci.* **26** 2790–3
James F and Roos M 1975 Minuit-a system for function minimization and analysis of the parameter errors and correlations *Comput. Phys. Commun.* **10** 343–67
Knoll G F 2010 *Radiation Detection and Measurement* (New York: Wiley)
Kowalsky R J, Johnston R E and Chan F H 1977 Dose calibrator performance and quality control *J. Nucl. Med. Technol.* **5** 35–40
NRC 1993 *Information Notice No. 93-10: Dose Calibrator Quality Control* ed commission USnr (Washington, DC: Office of Nuclear Material Safety and Safeguards) 20555
Saint-Gobain Crystals 2009 *Efficiency calculations for selected scintillators* (https://www.crystals.saint-gobain.com/sites/imdf.crystals.com/files/documents/efficiency-calculations_0.pdf)
Ten Haaf F and Verheijke M 1976 An improved gamma well counter for radioactive tracer applications *Int. J. Appl. Radiat. Isot.* **27** 79–84
Zanzonico P 2008 Routine quality control of clinical nuclear medicine instrumentation: a brief review *J. Nucl. Med.* **49** 1114–31

Design and performance of the micro-dose calibrator

supplemental material

Introduction

The following material supplements the effort documented in the manuscript titled “Design and performance of the micro-dose calibrator”. Please refer to the original manuscript for the full description of the work of designing and testing the performance of the micro-dose calibrator.

Electronics

The PMTs are operated using two different VME modules purchased from CAEN Electronics (Viareggio Italy). One is the VME V6533 high voltage controller used to power the PMTs. The V6533 can operate 6 HV channels independently so two VME modules were acquired to operate the 8 NaI/PMT detector modules. The second is the V1725 signal digitizer module which digitize the PMT anode signal at 250Ms/s (mega samples per second) with 14 bits of precision. The V1725 runs the Digital Pulse Processing for the Pulse Shape Discriminator (DPP-PSD) firmware. The firmware enables the V1725 to generate data packets of events, in which each data packet contains, among other data, the integral of the PMT anode pulse integrated over 800 ns and the time the constant fraction discriminator (CFD) trigger occurred. The pulse integral is used to generate the energy spectra and the trigger time is used to tag coincident pulses amongst the 8 detectors modules. To operate the micro-dose calibrator at the highest rates, two V1725 modules are used in parallel to reduce data bandwidth limitations. The two V1725 modules share a common clock through a clock distribution cable, ensuring time synchronicity between the two modules and the time stamps of the pulses acquired on either module can be used to tag coincident pulses accurately. A CAEN V1718 VME/USB bridge is used to provide VME bus cycles from the acquisition PC to operate the high voltage and digitizing VME modules via USB. A CAEN VME80084U VME create is used to house the two V6533 high voltage modules, the two V1725 digitizer modules and the V1718 VME/USB bridge. The CAEN A3818 dual link high speed fiber optic PCIe controller is used to acquire the signal data packets from the two V1725 digitizer modules allowing the simultaneous readout of the two modules independently while doubling the data acquisition bandwidth. A Supermicro based dual Xeon personal computer (PC) running Red Hat Enterprise Linux 6 (RHEL6) is used as the data acquisition computer. The PC has the A3818 dual link optical controller installed in one of its free PCIe slots. Refer to Figure 2 for photographs of the CAEN electronics.

Software

Software for a data acquisition and control system was developed to operate the CAEN high voltage and signal digitizer modules. The software was developed using two languages, Java and c/c++. The front end graphical user interface (GUI) and associated real time graphical displays, such as the PMT signal wave forms, energy and coincidence time spectra displays, were written in Java. The real time back end operation of the data acquisition system was written in c/c++. The backend was designed and written using an inhouse custom developed multi-threaded data buffer management system which manages the buffer transfer of data packets acquired from the V1725 modules through the various processing threads of the acquisition system. The processing threads of the backend are broken down into three types, acquisition threads, data merging thread, and data processing threads. There are two acquisition threads which read data from their individual V1725 module and stored into local buffers. These acquisition buffers are then passed through the buffer management system to a data buffer merging process thread. The merging thread receives data buffers from the two acquisition threads and merges the data packets in time order sequence into a new buffer which contains the data from all 8 detector modules within a certain time window. The time window width varies depending on the acquisition data rate and ranges from a 1 ms up to 1 s. Once the data buffer is assembled, the buffer is passed onto one of the data processing threads. The data processing thread unpacks the data from each event packet, performs the pipelined N-fold coincidence processing algorithm, and records associated energy and coincidence time spectra. A monitoring thread from within the GUI frontend collects the processed data from each of the processing threads, sums the various data components, and displays the resulting data as real time updated rate information, energy and time spectra and raw anode pulse wave forms from the PMT. Because the operation of the high voltage controllers does not require high bandwidth data throughput as does the data acquisition and processing required by the data acquired from the signal digitizing modules, a separate single thread coded in java and operating from within the GUI frontend is used to set and read the few control registers needed to adjust and monitor the high voltage settings for each detector module.

Pipeline coincidence processing algorithm

There are three primary data structures, one which contains the event data acquired from each of the eight detector modules, one which contains a list of pointers into the former data structure and a list type data structure containing information collected during the coincident tagging processing. The event data structure is made up of 8 event lists, one for each detector module. It is assumed that all the events in the event list are sorted sequentially in time. This avoids the need to search through the list for each data module to see if there are possible coincidence event anywhere in the event data list. The pointer data structure contains a pointer for each detector module event list. The algorithm starts by initializing all the pointers to reference the first event in the event list data structure as well as initializing the N-fold coincidence data list to hold 0 data elements. The algorithm then enters a loop which performs the following steps. Using the pointers referencing events from each detector module, the event with the minimum time is found. The time difference between the event with the minimum time and the rest of the events from every other detector module is calculated. The events which have a time difference less than ΔT are tagged and an N-fold coincidence is formed by saving the event data from each tagged event into a coincidence data structure and appended it onto the end of the coincidence list, the third data structure. For each of the events which was tagged as forming the N fold coincidence, including the event with the minimum time, their respective pointer, in the pointer data structure is incremented to point the next event. If no events are found to be in coincidence with the minimum time event, then a 1-fold coincidence (a unique single) event is recorded and added to the N-fold coincidence list and its corresponding pointer in the pointer data structure incremented to the next event. The algorithm then jumps back to the beginning of the loop and repeats until any one of the pointers referencing the event data list reaches the end of its list. The result is a list of coincidence events, each event corresponding to a single decay of the radioactive source placed inside the sampling well. Refer to Figure S1 below for a step by step walk through the algorithm

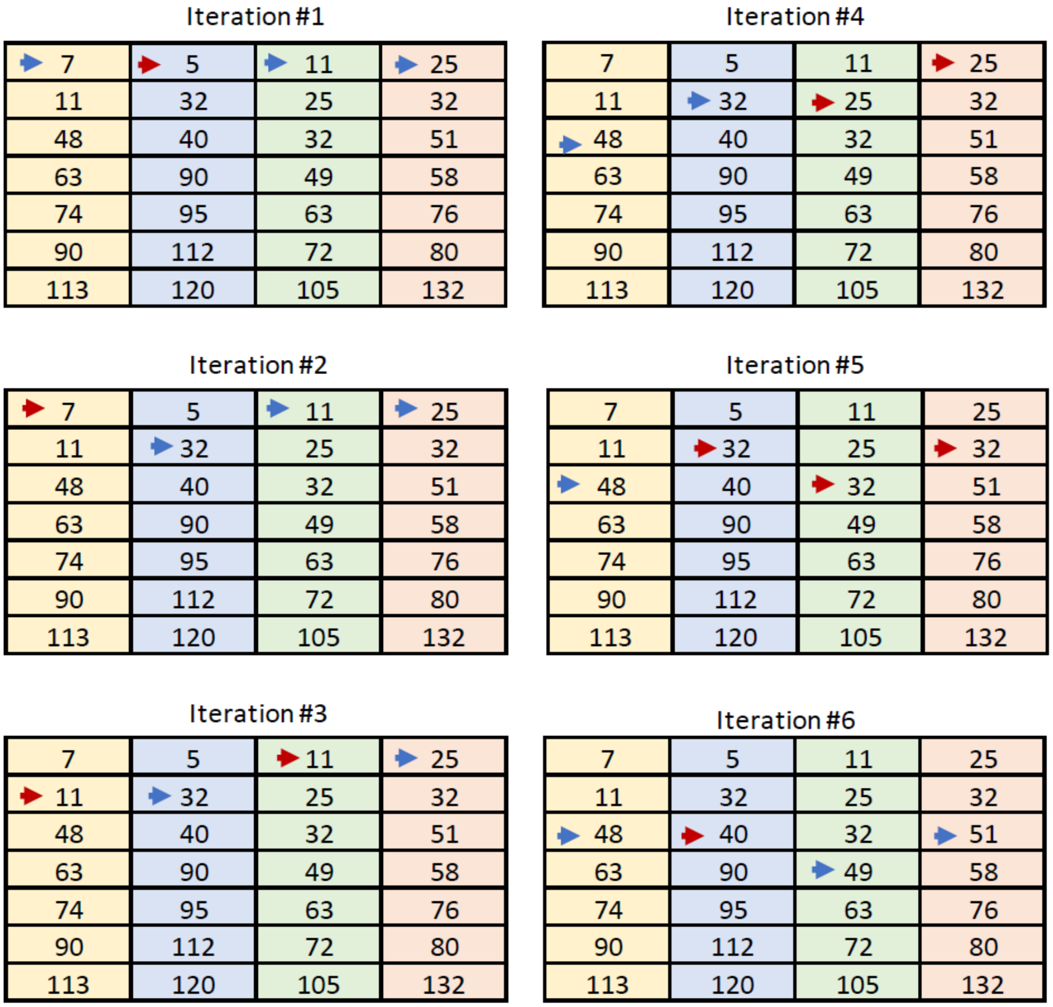

Iteration #1

➤ 7	► 5	➤ 11	➤ 25
11	32	25	32
48	40	32	51
63	90	49	58
74	95	63	76
90	112	72	80
113	120	105	132

Iteration #2

► 7	5	➤ 11	➤ 25
11	➤ 32	25	32
48	40	32	51
63	90	49	58
74	95	63	76
90	112	72	80
113	120	105	132

Iteration #3

7	5	► 11	➤ 25
► 11	➤ 32	25	32
48	40	32	51
63	90	49	58
74	95	63	76
90	112	72	80
113	120	105	132

Iteration #4

7	5	11	► 25
11	➤ 32	► 25	32
➤ 48	40	32	51
63	90	49	58
74	95	63	76
90	112	72	80
113	120	105	132

Iteration #5

7	5	11	25
11	► 32	25	► 32
➤ 48	40	► 32	51
63	90	49	58
74	95	63	76
90	112	72	80
113	120	105	132

Iteration #6

7	5	11	25
11	32	25	32
➤ 48	► 40	32	➤ 51
63	90	➤ 49	58
74	95	63	76
90	112	72	80
113	120	105	132

Figure S1. A six-iteration example of the pipelined coincidence processing algorithm using a coincidence time window of 0. Each table displays the event time stamp in arbitrary units for 4 detector modules (#1-#4) arranged in columns left to right (column #1 through #4) in ascending order for six iterations of the algorithm. At iteration #1, the pointers are initialized to point to the beginning of the event list. The minimum time stamp is located as indicated with a red arrow for detector #2. At the end of iteration #1, no coincident events are found since the coincidence time window is set to 0 and detector #2 is tagged with a unique single event at time 5 and the pointer is incremented by one. At iteration #2, a unique single event is tagged for detector #1 at time 7, the detector module with the minimum time stamp. At the end of iteration #2, the event pointer is incremented for detector #1. The first 2-fold coincident event is tagged at iteration #3. The minimum time stamp is 11 with two detectors having events the same time stamp. After the coincident event is tagged, the event pointers for both detectors #1 and #3 are incremented. At iteration #4 a 2-fold coincident event is tagged at time 25 between detectors #3 and #4. The pointers for detectors #3 and #4 are then incremented. At iteration #5 a 3-fold coincidence is tagged between detectors #2, #3 and #4, after which the pointers for these detectors are incremented. At iteration #6, the detector with the minimum time stamp is detector #2 and its unique single 1-fold coincident event. The algorithm continues until any one of the pointers reaches the end of its list.

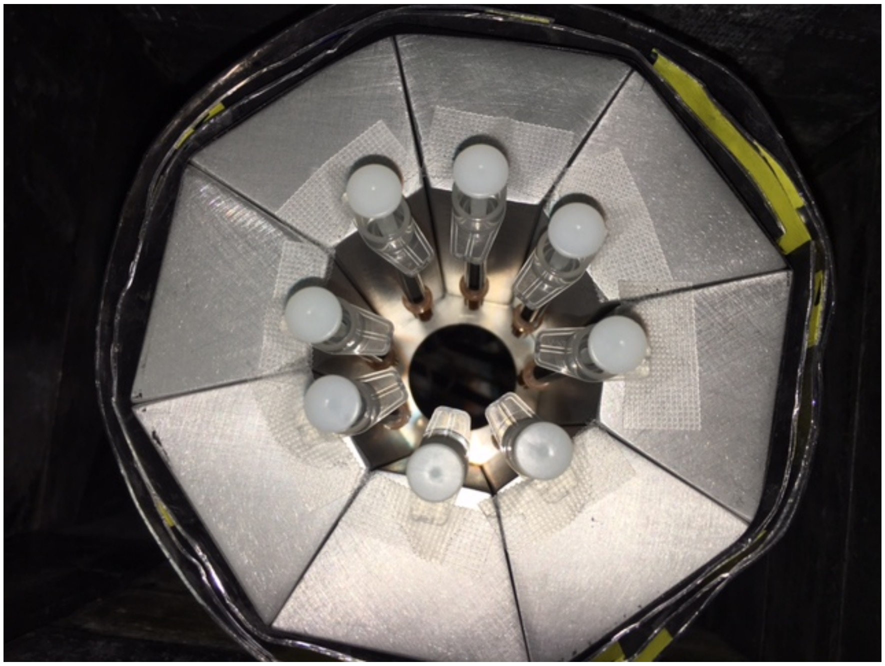

Figure S2. The 8 syringe setup for the coincidence time resolution study. 8 syringes filled with a 50 µL solution containing 1 µCi of 18F were placed on the surface of each of the 8 detector modules of the micro-dose calibrator. The goal was to generate as many lines of response possible thus generating well measured coincidence time spectra between all detector pair modules. In this current setup, adjacent detector pair modules were not able to properly form lines of response so they were omitted from the coincidence time resolution study.

Decoupling individual detector timing jitter from two detector coincidence time resolution

The timing resolution is defined as the standard deviation of the overall timing jitter of the detector module defined as σ_i for the ith detector module. The method of measuring the timing jitter σ_i involves measuring the FWHM of the coincidence time distribution of three pairs of detector modules which are in coincidence, and then solving the linear equation which equates the width of the coincidence timing distribution into their individual contribution to its width. If the timing jitter distributions for each individual detector module are Gaussian this would result in a Gaussian coincidence time distribution. Further assuming the width of the coincidence timing distribution is determined by the quadratic sum of the individual timing jitter contributions of each of the detector modules in coincidence, then if one has a set of three detector modules, with all three detector modules in coincidence with each other, one can form the following set of linear equations

$$\begin{aligned}\sigma_{12} &= \sqrt{\sigma_1^2 + \sigma_2^2}\\ \sigma_{13} &= \sqrt{\sigma_1^2 + \sigma_3^2}\\ \sigma_{23} &= \sqrt{\sigma_2^2 + \sigma_3^2}\end{aligned} \tag{S1}$$

which has the following solution for each individual jitter contribution

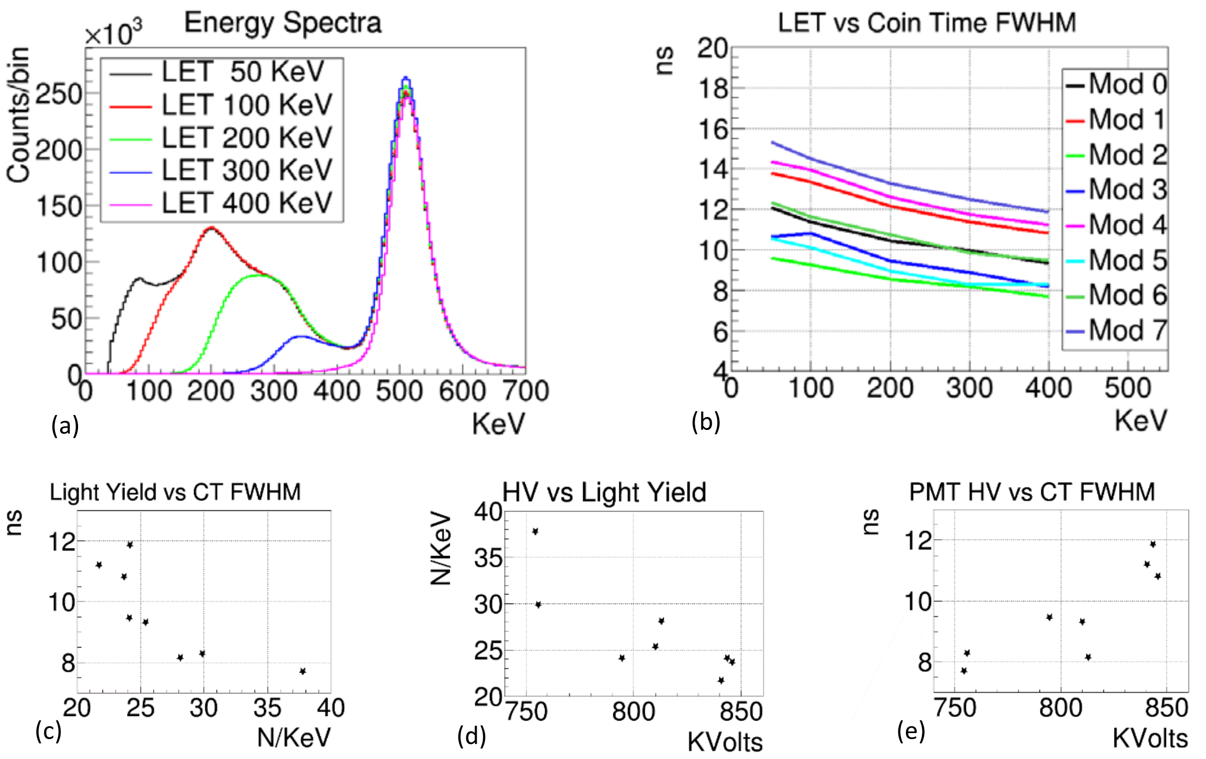

Figure S3. The results of the coincidence timing resolution study are shown in figures S3(a) and S3(b). Figure S3(a) plots superimposed energy spectra of a ^{18}F solution with each spectrum having a different lower energy threshold setting. Figure S3(b) plots the coincidence time distribution FWHM for each individual detector module as a function of the lower energy threshold. As expected, the FWHM decreases as the lower energy threshold increases. Figures S3(c), S3(d) and S3(e) show correlation plots of NaI scintillation light yield in number of photons per keV (N/keV), Coincidence Time FWHM and PMT high voltage setting. The inverse correlation between the light yield and the coincidence timing resolution is shown in figure S3(c). Figures S3(d) and S3(e) show the correlations between the high voltage setting and light yield and coincidence time resolution respectively.

$$\begin{aligned} \sigma_1 &= \sqrt{(\sigma_{12}^2 + \sigma_{13}^2 - \sigma_{23}^2)/2} \\ \sigma_2 &= \sqrt{(\sigma_{12}^2 + \sigma_{23}^2 - \sigma_{13}^2)/2} \\ \sigma_3 &= \sqrt{(\sigma_{13}^2 + \sigma_{23}^2 - \sigma_{12}^2)/2} \end{aligned} \qquad (S2)$$

Furthermore, the FWHM of the coincidence timing distribution for detector pair ij is related to the standard deviation assuming the distribution is gaussian as follows

$$FWHM_{ij} = 2\sqrt{2\ln 2}\,\sigma_{ij} \qquad (S3)$$

Therefore, one measures the FWHM of the coincidence timing distributions for all detector pairs in coincidence and from all the combinations of each detector pair, one can then generate several measures of the timing jitter (σ_i) for detector module i and from these measurements, an average jitter and its standard deviation can be obtained. For example, for detector module 1, which is in coincidence with detector modules 2 – 8, the following combinations of detector pair combinations are formed.

$$
\begin{array}{lll}
\sigma_1=\sqrt{(\sigma_{12}^2+\sigma_{13}^2-\sigma_{23}^2)/2} & \sigma_1=\sqrt{(\sigma_{12}^2+\sigma_{14}^2-\sigma_{24}^2)/2} & \sigma_1=\sqrt{(\sigma_{12}^2+\sigma_{15}^2-\sigma_{25}^2)/2} \\
\sigma_1=\sqrt{(\sigma_{12}^2+\sigma_{16}^2-\sigma_{26}^2)/2} & \sigma_1=\sqrt{(\sigma_{12}^2+\sigma_{17}^2-\sigma_{27}^2)/2} & \sigma_1=\sqrt{(\sigma_{12}^2+\sigma_{18}^2-\sigma_{28}^2)/2} \\
\sigma_1=\sqrt{(\sigma_{13}^2+\sigma_{14}^2-\sigma_{34}^2)/2} & \sigma_1=\sqrt{(\sigma_{13}^2+\sigma_{15}^2-\sigma_{35}^2)/2} & \ldots
\end{array}
\qquad (S4)
$$

for a total of 21 combinations. Because measuring a coincidence distribution between adjacent detectors proves difficult, the number of non-adjacent detector pair combinations reduces to 6.

To best study the overall timing jitter of the detector module and its dependence on the lower energy threshold (LET) setting, coincidence timing spectra were obtained for the LET settings of 50, 100, 200, 300 and 400 keV.

In acquiring the coincident timing spectra, eight syringes were filled with 50 µL solution containing 1 µCi of an ^{18}F. Each syringe was placed at the surface of each detector module to generate as many coincidence detector pairs as possible. See Figure S1.

Figures S3(a) and S3(b) show the effects of changing the lower energy threshold on the energy spectrum. The left graph shows the energy spectra plots superimposed for each lower energy threshold setting with the lower energy threshold setting of 400 keV preserving most of the gammas which underwent a photoelectric interaction with an electron within the NaI crystal. For each lower energy threshold setting, coincidence time distribution spectra were collected for all detector pairs and their FWHM measured. Using the technique to derive the individual detector module time jitter σ_i describe above, the equivalent FWHM$_i$, equal to $2\sqrt{2\ln 2}\,\sigma_i$, is then plotted vs the lower energy threshold setting for all eight detector modules in figure S3(b). This graph shows the dependence of the timing resolution as a function of lower energy threshold showing an inverse relation as expected. For the lower energy threshold setting of 400 keV, the range of detector module timing resolution FWHM is from 7.7 ns to 11.9 ns with an average of 9.6 ns +/- 1.5 ns (CV 16.1%).

The bottom row of graphs in Figure S3 summarize the correlations between the detector module high voltage setting, the energy resolution and scintillation light yield measured as the number of scintillation photons (N) per keV. The data presented are only from the 400 keV lower energy threshold setting. The light yield ranges from a minimum of 21.7 N/keV to a maximum of 37.8 N/keV with an average of 26.9 N/keV +/- 5.1 N/keV (CV 19.0%). Using the photopeak gaussian sigma to calculate the energy coefficient of variation (E_{CV}), the light yield was then calculated as $N/keV = 1/(661\ E_{CV}^2)$.

Randoms Study

A randoms study was performed of just the two detector coincidence randoms contribution and the results are shown in the graphs displayed in Figure S4. Using the data collected from the linearity studies, a coincidence time distribution plot was generated when there was 3.4 MBq of ^{18}F activity in the sampling well. This is shown figure S4(a). A red line indicates the randoms contribution to the

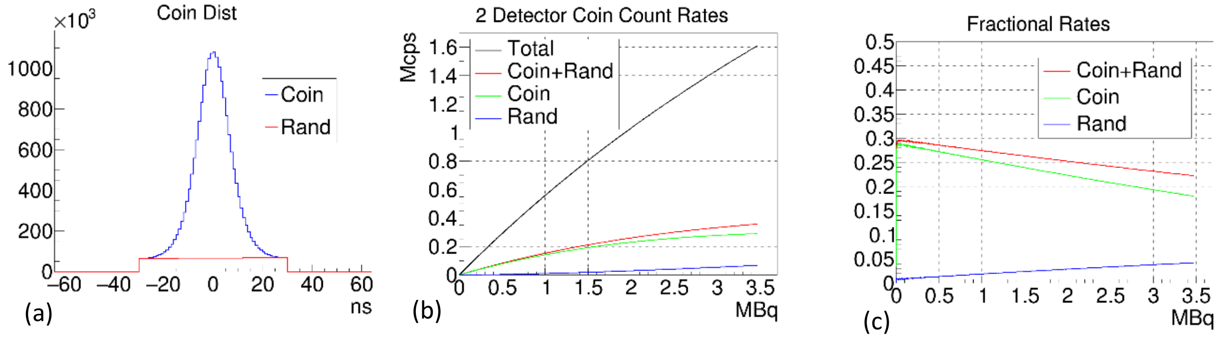

Figure S4. The results of a randoms study for two detector pair coincidence rates. Figure S4(a) plots the coincidence and randoms contribution to the total coincidence time distribution spectra for ^{18}F activity of 3.4MBq. A tail extrapolation method is used to calculate the randoms contribution to the total coincidence distribution spectra which can be shown in the red plot. Figure S4(b) plots ^{18}F activity in MBq vs count rates in Mcps for the total correlated count rates, the total two detector coincidence count rate which includes both the coincidence and randoms contribution, just the coincidence contribution and just the randoms. Figure S4(c) plots the ^{18}F activity in MBq vs the fractional contribution to the total correlate count rate of the total two detector coincidence rate, just the coincidence rate and just the randoms rate. The data shows a rate dependence on the fractional contribution of the two detector coincidence rate to the total correlated count rate. It also shows that at 3.4MBq, the fractional contribution of the randoms is 4% that of the total correlated count rate.

coincidence time distribution using a tail extrapolation algorithm. This analysis was repeated for each time sample and plots of ^{18}F activity vs total correlated count rate, two detector total coincidence count rate, just coincidence and just randoms count rate. This data is plotted in figure S4(b). Figure S4(c) plots ^{18}F activity vs the ratio of total coincidence rate, just coincidence and just randoms rate to total correlated count rate. From figure S4(c), one can see that the fractional contribution of the randoms rate at the highest ^{18}F activity of 3.4 MBq is 4.2%, which makes this a small contribution and leads to a small correction to the total correlated count rate. Furthermore, due to the empirical nature of the pulse pileup dead time correction model, effects such as randoms contribution are effectively included in the correction. Therefore, the large coincidence time window should not be of concern regarding the ability of the micro-dose calibrator to operate at 3.4 MBq and maintain linearity within a ±1% accuracy window. Future work will study the randoms contribution in more detail with a goal of including a singles based randoms correction to the total correlated count measurement, for which the pulse pile up dead time correction model will need to be revised.